Heterogeneous & Homogeneous & Bio- & Nano-

CHEMCATCHEM

CATALYSIS

Accepted Article

Title: Photocatalytic hydrogen production by boron modified TiO2 / carbon nitride heterojunctions

Authors: Konstantinos C Christoforidis, Tiziano Montini, Maria Fittipaldi, Juan Josè Delgado Jaén, and Paolo Fornasiero

To be cited as: *ChemCatChem* 10.1002/cctc.201901703

Link to VoR: http://dx.doi.org/10.1002/cctc.201901703

A Journal of

ChemPubSoc Europe

WILEY-VCH

www.chemcatchem.org

Photocatalytic hydrogen production by boron modified TiO_2 / carbon nitride heterojunctions

Konstantinos C. Christoforidis[a],[b],[c]*, Tiziano Montini[b], Maria Fittipaldi[d], Juan Josè Delgado Jaén[e] and Paolo Fornasiero[b]*

Abstract: Boron-doped anatase TiO_2 particles were effectively coupled with carbon nitride (CN) forming nanocomposites. The materials were fully characterized by DR-UV-Vis, N_2 adsorption-desorption isotherms, XRD, Raman, FTIR, TGA, XPS, TEM, electron energy loss spectroscopy, photoluminescence, and electron paramagnetic spectroscopy (EPR) spectroscopy. The developed heterojunctions were applied as photocatalysts for hydrogen (H_2) evolution by the photoreforming process of ethanol under solar irradiation, using minimal amount of Pt nanoparticles (0.1 wt.%) as co-catalyst. The effects of boron addition and CN content were evaluated and optimized nanocomposite presented 85% increase in H_2 evolution compared with the pure anatase TiO_2 catalyst. The observed higher H_2 evolution rates were ascribed to improvements in charge formation and separation efficiency due to the B-dopant and the presence of CN.

Introduction

Clean energy supply with no carbon-footprint is one of the most critical challenges the scientific community is facing. This need originates from the severe environmental impact of traditional fossil fuel usage through the production of greenhouse gases together with their progressive depletion. Semiconductor photocatalysis and in particular the field of solar fuels, is currently considered as one of the most practical candidates to provide sustainable clean energy[1]. From the variety of solar fuels presented in the literature including fuels derived from CO_2 conversion, photocatalytic H_2 production from water or bioavailable substrates is considered one of the most promising processes able to deal with both sustainable clean-energy supply and reduction of greenhouse gas emissions[1a, 1b].

[a] Dr. K.C. Christoforidis. Department of Environmental Engineering, Democritus University of Thrace, Vasilisis Sofias 12, 67100 Xanthi, Greece. E-mail: kochristo@env.duth.gr
[b] Dr. K.C. Christoforidis, Prof. T. Montini, Prof. P. Fornasiero. Department of Chemical and Pharmaceutical Sciences, ICCOM-CNR and INSTM University of Trieste, Via L. Giorgieri 1, 34127 Trieste, Italy. E-mail: pfornasiero@units.it
[c] Dr. K.C. Christoforidis. Institut de Chimie et Procédés Pour l'Energie, l'Environnement et la Santé, (ICPEES) ECPM, University of Strasbourg, 25 rue Becquerel Cedex 2, Strasbourg, France.
[d] Prof. M. Fittipaldi. INSTM and Department of Physics and Astronomy, via Sansone 1, University of Florence, via della Lastruccia 3-13, 50019 Sesto Fiorentino (FI), Italy.
[e] Dr. J.J. Delgado Jaén. Departamento de Ciencia de los Materiales e Ingeniería Metalúrgica y Química Inorgánica, Facultad de Ciencias, Universidad de Cádiz, Campus Río San Pedro, 11510, Puerto Real, Cádiz, Spain.

Supporting information for this article is given via a link at the end of the document.

Among the different catalysts applied in photocatalytic H_2 production process either from pure water splitting or the photoreforming of carbohydrates, TiO_2 is the most studied[1a, 1d, 2]. This originates from the TiO_2 inherent properties such as low cost, chemical inertness and non-toxicity. Unfortunately, pure TiO_2 is active only under UV-light irradiation and presents fast charge recombination rates. Different approaches have been applied to deal with these limitations including doping with metal and non-metal elements [2-3] as well as the development of heterostructures and heterojunctions [1a, 2]. Among the different dopants used to improve the properties of TiO_2, boron is an attractive candidate since B-doped TiO_2 has shown improvement in photoactivity under either UV[4] or visible light irradiation[5] as well as improvements in light absorption and formation of photogenerated charges[4, 6]. Over the last years, carbon nitride (CN) has been also established as a promising catalyst in solar fuels production processes[1a, 7]. CN is a metal-free, visible light active semiconductor with relatively high conduction band edge potential (~-1.12 eV vs. NHE)[7d]. However, bulk CN presents moderate photoactivity mainly due to the fast charge recombination rates [8]. Therefore, modification of the parent material is required to achieve reasonable activity[1a, 7c, 7e, 8c, 9]. Further on the development of efficient photocatalyst for H_2 production, the formation of a heterojunction has been also shown as an efficient route to prevent charge recombination in semiconductors and to improve light absorption properties[1a, 10]. This is accomplished via charge separation in the different phases of the heterojunction through the formed interface/junction and the coupling of wide with narrow band gap semiconductors[1a, 2, 3b, 11]. In this direction, heterojunctions made of TiO_2 and CN have been effectively applied in a variety of photocatalytic reactions[3b, 12].

In the present study we performed a combined modification through a) the development of nanocomposites made of CN and anatase TiO_2 for the construction of heterojunctions and b) doping of anatase TiO_2 with boron. The prepared materials were fully characterized and applied as photocatalysts in H_2 production from the photoreforming of ethanol under simulated solar irradiation. Both boron and CN improved significantly H_2 evolution compared with pure TiO_2. Finally, the mechanism of activity is discussed on the bases of the catalytic and spectroscopic data.

Results and Discussion

The structure of TiO_2 and CN were assessed by XRD. The XRD patterns are given in Figure 1. The TiO_2 was in the anatase phase (JCPDS: 21-1272) in all prepared materials: the pure TiO_2 sample, the TiCN*x* and TiCN5B*y* series. It has been shown previously that the TiO_2 crystal form is not affected by either the presence of CN or boron as a dopant [3b, 12b]. However, the presence of boron somehow affected the XRD patterns of the TiCN5B*y* samples. Increasing the nominal boron content in the TiCN5B*y* series results in a broadening of the diffraction peaks. This implies a decrease of the TiO_2 crystallite size/crystallinity. The anatase crystallite sizes of all samples extracted using the Scherrer equation are presented in Table 1.[13] This indicates that doping with small amounts of boron brings a distortion in the anatase structure in accordance with the literature[14]. The actual B/Ti molar ratio has been determined from ICP-AES results, observing that it is significantly lower than the nominal one: 0.71 for TiCN5B5, 1.22 for TiCN5B10, 2.19 for TiCN5B20 and 1.14 for TiCN0B10. Notably, these results are in agreement with reports on B-doped TiO_2 materials[15] and could be rationalized considering that H_3BO_3 is highly volatile and undergoes to decomposition to B_2O_3 even at the mild temperature employed during calcination of the present materials (350°C). Consistently, the minor differences in the XRD observed upon B doping are related to the low amount of incorporated B. The CN XRD pattern exhibit two characteristic reflections at approximately 13 °C and 27.4 °C corresponding to the (1 0 0) (interplanar spacing of the tri-s-triazine unit) and (0 0 2) (interlayer stacking) crystal planes of CN [7b]. These two features confirmed the successful formation of CN under the conditions applied [9d]. However, no diffraction peak corresponding to CN was observed in the nanocomposites. This probably originates from the low amount of CN used.[9d]

Raman spectra of the un-doped and boron doped TiO_2/CN composite samples (Figure 2) agree well with XRD results showing the exclusive presence of the anatase structure with peaks at ca. 144.8, 196, 399, 518 and 640 cm^{-1}, corresponding to the $E_g(1)$, $E_g(2)$, $B_{1g}(1)$, $B_{1g}(2)$, $A_{1g}(1)$ and $E_g(3)$ modes,

Table 1. BET surface area, crystallite size and CN content of the prepared materials.

Catalyst	BET surface area (m^2/g)	Crystallite size (nm)[a]	CN % wt.[b]
TiO_2	69.8	15.1	–
TiCN2	64.4	15.7	0.6
TiCN5	70.6	15.9	1.3
TiCN7	77.9	15.1	1.9
TiCN10	72.6	15.1	4.2
TiCN5B5	79.6	16.2	1.3
TiCN5B10	108.5	13.3	1.1
TiCN5B20	120.8	12.0	1.2
TiCN0B10	69.9	16.4	–
CN	86.9	–	–

[a] calculated using the Scherrer equation and the (1 0 1) diffraction peak of anatase. [b] Extracted from TGA.

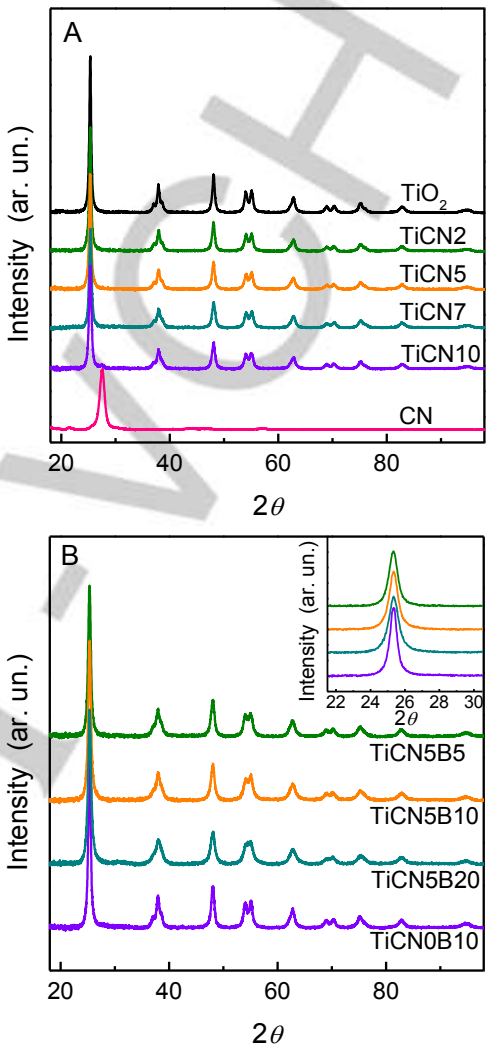

Figure 1. XRD patterns of the TiCN*x* (A) and the TiCN5B*y* series (B).

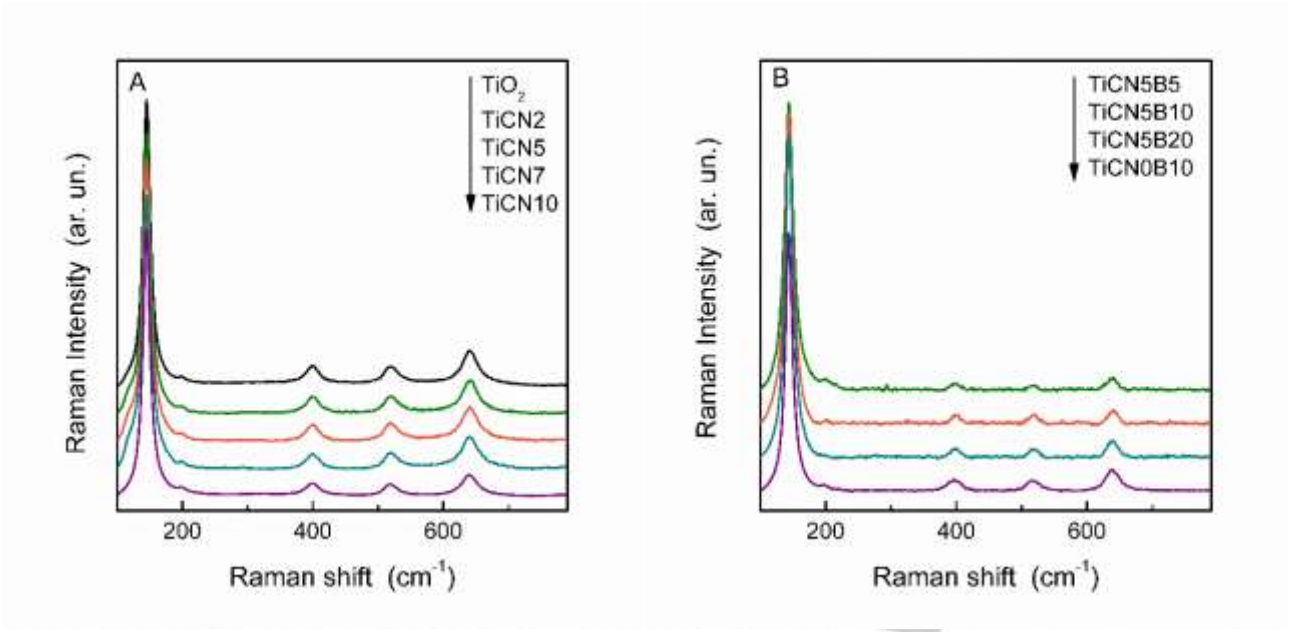

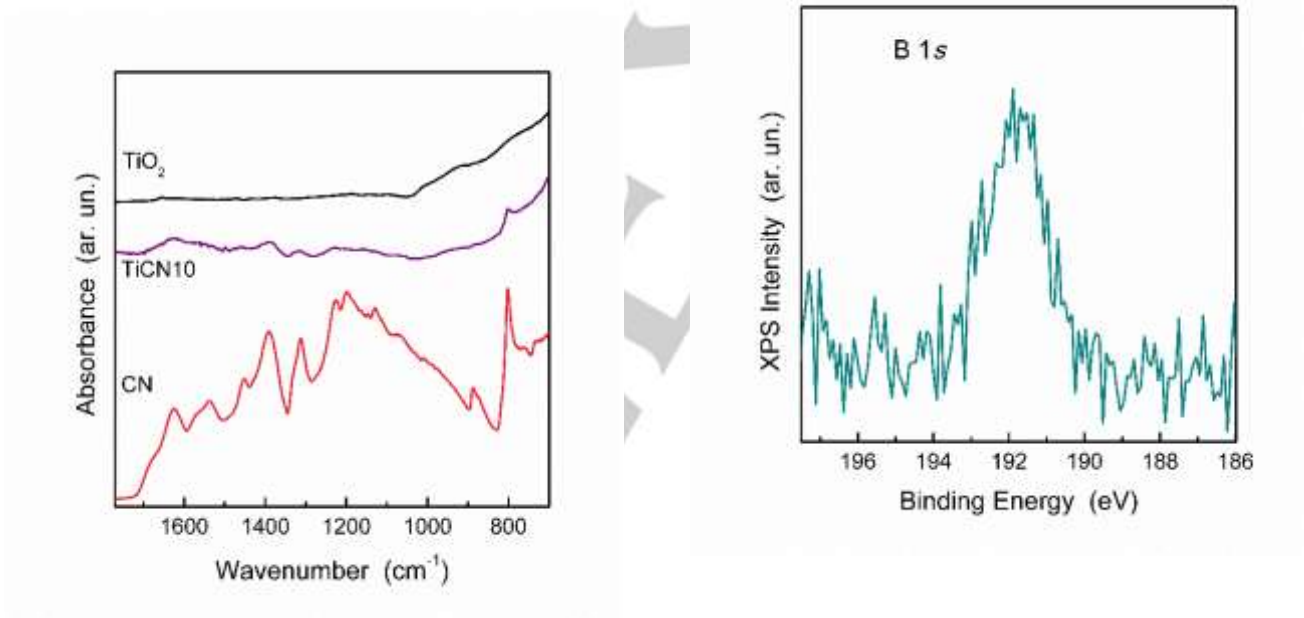

Figure 2. Raman spectra of the TiCN*x* (A) and the TiCN5B*y* series (B).

Figure 3. FTIR spectra of the pure TiO_2 and CN catalysts and the TiCN10 composite.

respectively.[3a] CN does not affect the spectral characteristics. However, boron induces a small shift of the $E_g(1)$ mode towards lower wavenumbers (i.e. 144 cm^{-1}, Figure S1). This may originate from the presence of crystalline defects in the TiO_2 framework due to the presence of boron[16]. No peaks corresponding to CN were detected, probably due to the low CN concentration. Since no evidence was given for the presence of CN in the composite materials using either XRD or Raman, Fourier Transform Infrared

Figure4. High resolution XPS spectrum of the TiCN5B20 sample in the B 1*s* region.

Spectroscopy (FTIR) was applied to verify the presence of CN in the composite. CN showed the expected band vibrations (Figure 3). The characteristic stretching vibration modes of the heptazine ring are observed in the 1200-1680 cm^{-1} region, confirming the presence CN.[7b, 17] The CN bands were detected only in the composite with the highest CN content (TiCN10). Such data

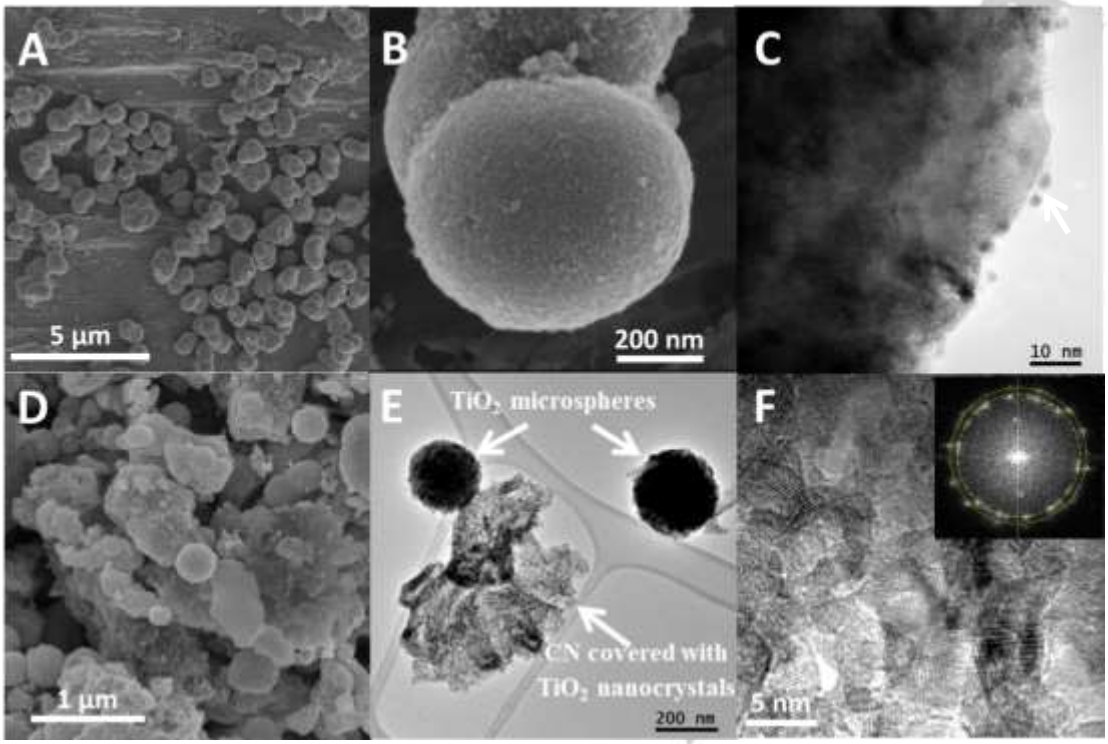

Figure 5. SEM images of the pure TiO2 sample (A-B) and TiCN5B10 composite (D). HRTEM of the pure TiO2 (C), as well as the TiCN5B10 catalyst (E-F) are also included. The Pt particles are indicated with the arrow in panel C.

suggest that the CN structure is maintained during the hybridization process.

To verify the presence of boron and to further elucidate the surface composition and chemical state of the prepared materials XPS was applied. Peaks attributed to Ti, O, C, and N are detected in the XPS survey spectra (Figure S2). High resolution XPS spectra are given in Figure S3. For all materials, the peaks centered approximately at 458.5 and 464.3 eV are ascribed to the Ti $2p_{3/2}$ and $2p_{1/2}$ spin-orbit components of Ti^{4+} surface species on anatase TiO_2[18]. The characteristic C 1*s* and N 1*s* peaks of CN were detected at 288.4 and 398.5 eV, respectively[18]. The presence of boron is verified by the peak centered at approximately 191.9 eV that is attributed to the B 1*s* (Figure 4)[19]. Boron peaks in this region have been suggested to occupy interstitial positions[19]. No peaks attributed to H_3BO_3 and B_2O_3 were detected,

The composition and the stability of the materials under thermal treatment were examined using TGA. The TGA profiles of all materials are given in Figure S4. Pure CN is decomposed at temperatures higher than 570 ◦C. On the contrary, the onset for all hybrid materials is observed at lower temperatures, approximately at 500 ◦C. This verifies the stability of the composite materials under the thermal treatment applied for the calcination step of the TiO_2 phase at 350 ◦C. The content of CN in the composite materials was calculated from the weight remained and is given in Table 1.

In addition to the above techniques that give information on the bulk structure and composition of the hybrids, morphological features and the verification of the coupling of the two materials were studied using SEM and TEM. TEM images were taken from the used catalysts after the photocatalytic reaction. Figure 5 shows representative SEM and TEM images of the pure TiO_2 sample (Figure 5A, B and C). A nearly perfectly spherical morphology is observed although no template was used in the synthesis process. The size of the microspheres ranges between ca. 0.6 and 1.1 µm and are composed of interconnected TiO_2 nanocrystals. Figure 5B clearly shows the porosity of the microspheres. The Pt nanoparticles with size in the range of 2-3 nm are also observed in Figure 5C. TiO_2 microspheres are also observed in the TiO_2/CN composites. However, the size of the TiO_2 microspheres (0.2 to 0.5 µm) is significantly smaller compared with the bare TiO_2 sample. In the case of the composite, in addition to the TiO_2 microspheres, CN structures covered with

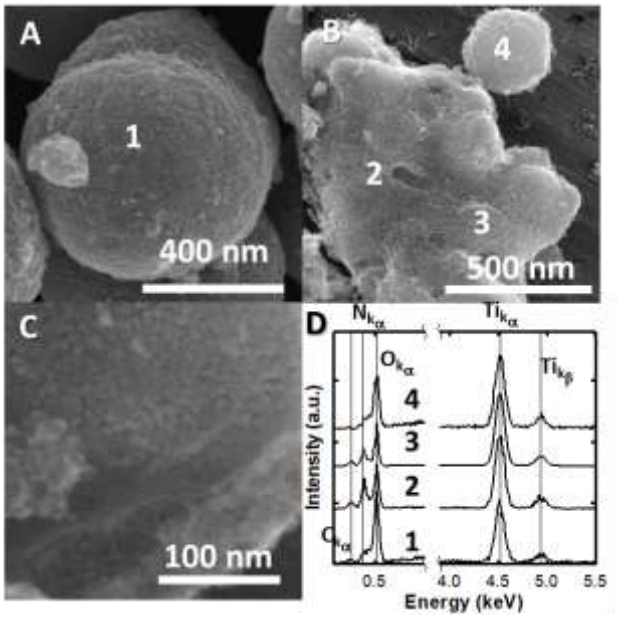

Figure 6. SEM images of pure TiO_2 (A) and TiCN5B10 (B-C) indicating the areas where the EDS spectra included in (D) were recorded.

TiO_2 nanocrystals are also observed (Figure 5E). Figure 5F clearly shows that 5-10 nm nanoparticles of TiO_2 are randomly decorating the CN sheets. The decrease of the microspheres size in the composite materials compared with the pure TiO_2 can originate from the deposition of TiO_2 nanocrystals on CN in the second case. The digital diffraction pattern of the full image shows many spots forming two cycles that corresponds 2.3 and 1.9 Å. Unfortunately, these spacing can't be univocally assigned to anatase and others TiO_2 phases cannot be excluded. This result can be interpreted considering that CN nanosheets are covered by TiO_2 crystals with different orientations. Interestingly, one single spot is observed for a spacing of 3.4 Å, which may be due to the (002) family of planes of CN where the TiO_2 nanoparticles are anchoring. Additionally, small CN sheets are also detected at the edges of the TiO_2 microspheres (Figure 5E). It must be highlighted that the TEM images correspond to the used catalysts. Thus, the detection of CN structures covered with TiO_2 nanocrystals after the photocatalytic test indicates a stable and strong interaction between the two phases.

Energy dispersive X-ray spectra (EDS) was used to confirm the intimal interaction of both phases. Figure 6D includes the EDS spectra obtained in the areas marked with number in the SEM images (Figure 6A and B). According to the spectra 1 and 4, we can observe that TiO_2 microspheres are composed by Ti and O in both the pure titania and the composite samples. It must be mentioned that both spectra show a small contribution at ~0.45 eV that correspond to the L-level emission lines of Ti and not to the K_a emission of nitrogen that is observed at 0.39 eV. The analysis performed on others areas of the composite sample show the presence of Ti, O, C and N. This is in good concordance with the assumption that the CN sheets are covered with TiO_2 nanocrystals. This is well illustrated by the higher magnification SEM image of this area included in figure 6C.

The textural properties of the materials were studied using nitrogen physisorption isotherms (Figure S5) since surface area is very important in photocatalytic applications. Pure TiO_2 presents a mesoporous structure typical for TiO_2 nanoparticles[20]. Bare CN presents a hysteresis loop at high partial pressures ($0.9 < P/P_0 < 1$) which probably originates from pores formed through the assembly of secondary particles. The presence of CN induced small changes in the nanocomposites compared with the pristine TiO_2, increasing slightly the BET surface area. However, as indicated by the N_2 adsorption-desorption isotherms, materials containing CN show higher absorption capability at high partial pressure. The introduction of boron in the anatase structure induced an increase in the surface area. This is manifested in the sample prepared using the highest boron concentration and is linked with the lower crystallinity observed with XRD. The same trend in surface area with varying B-content has been previously observed for B-doped TiO_2 materials prepared under similar conditions in the absence of CN[20].

Photocatalytic H_2 production from aqueous ethanol solution was performed under simulated solar light irradiation and H_2 evolution was monitored for a period of 24 h under flow conditions. The corresponding data are presented in Figure S6. The linearity observed over 24 h verify the stability of the prepared materials under the catalytic conditions applied. To further establish the stability of the prepared catalyst, the XRD and FTIR spectra of the post reaction catalyst were also recorded for the TiCN5B10 case (Figure S7). Figure 7 shows H_2 production rates using the TiCN*x* (Figure 7A) and the TiCN5B*y* (Figure 7B) catalysts. Pure CN presents approximately 20 times lower H_2 production (ca. 0.053mmol g^{-1} h^{-1}) than pure TiO_2 under identical conditions. Therefore it is not included in the data presented in Figure 7. In the TiCN*x* series a small variation in H_2 evolution is observed by varying the CN content. H_2 evolution presents a volcano-type dependence on CN content. Activity is improved until the CN content reaches 5%. Further increase of the CN amount results in a decrease in activity. The optimized TiCN5 composite presents ca. 12% higher activity than the pure TiO_2 catalyst. This most likely originates from the formation of a heterojunction that allows efficient charge separation as previously suggested in similar TiO_2/CN composites [1a, 3b, 18, 21].

The effect of B doping was studied on the optimum CN content (i.e. 5% CN). As illustrated in Figure 7B, the introduction of boron results in improved H_2 evolution. The TiCN5B10 composite presents the highest activity corresponding to an 85% and 66% improvement in H_2 production compared with the pure TiO_2 and the TiCN5 catalyst, respectively. It is noted that in both series the same trend in the activity is observed when considering the surface area of the catalyst. However, the increase in activity drops from 85% to 20%. A photocatalytic reaction under pure visible light irradiation ($\lambda > 420$ nm) was also

performed using the most active TiCN5B10 catalyst. Under these conditions no H_2 production was detected.

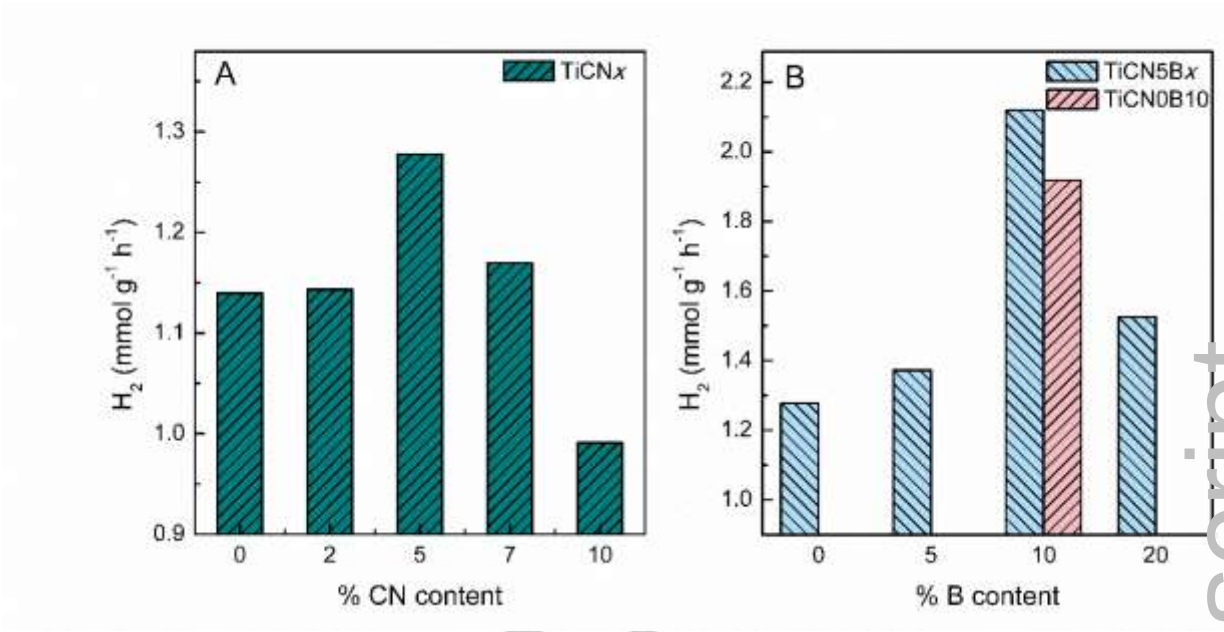

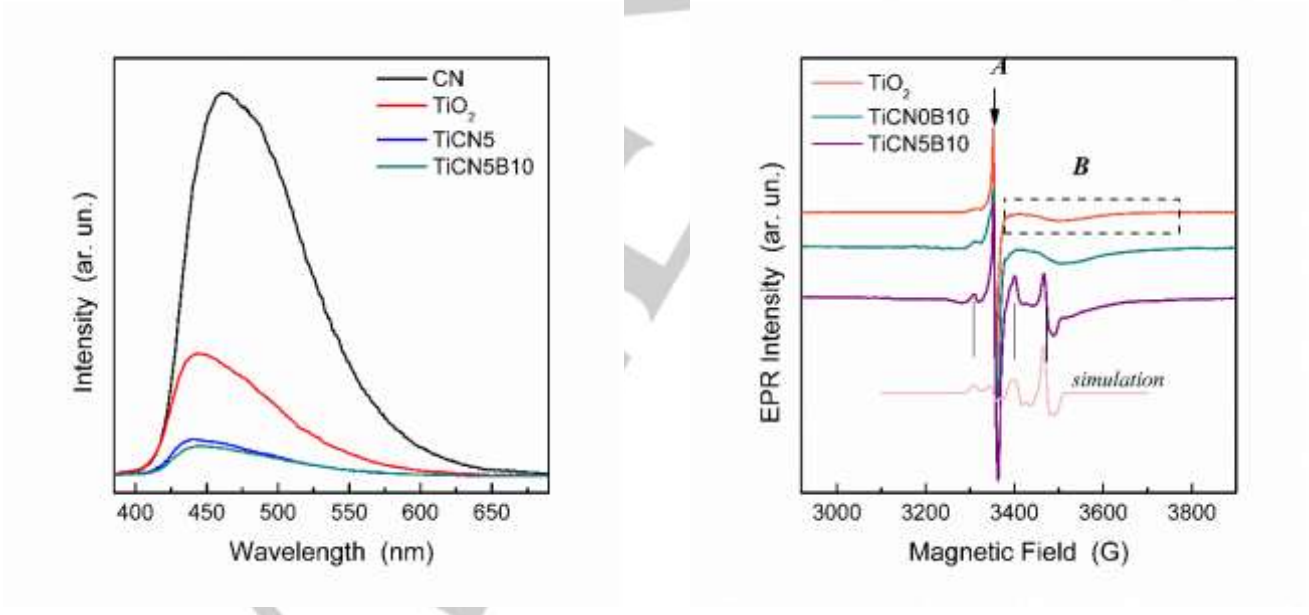

Figure 7. Photocatalytic H_2 evolution using the TiCN*x* (A) and the TiCN5B*y* composites (B).

Figure 8. Photoluminescence emission spectra of the pure CN and TiO_2 and the TiCN5 and TiCN5B10 composite materials.

To investigate the role of CN and boron on photoactivity photoluminescence, EPR and DR-UV-Vis spectra were collected. The DR/UV-Vis spectra are shown in Figure S8. TiO_2 absorbs light only in the UV region presenting band gap energy (E_g) of 3.22 eV (Figure S8C). On the other hand, CN absorbs light at longer wavelengths with E_g approximately at 2.8 eV. As expected, the CN in the composite materials increases light absorption in the visible region (Figure S8A). Boron does not affect the band

Figure 9. EPR spectra of the pure TiO_2, TiCN0B10 and TiCN5B10 catalysts taken under irradiation.

gap energy (E_g ~ 3.20 eV) but a small increase in light absorption in the visible region is detected (Figure S8B)[22]. These data clearly indicate that modification of TiO_2 with boron and coupling with CN expands light absorption which could be beneficial in photocatalysis.

Besides light absorption, formation of photogenerated charges and charge recombination are also important properties since they are directly related with the photocatalytic performance. PL emission spectra have be used to give an estimation of the charge separation efficiency in TiO_2 and CN based materials [3b, 17], although the mechanism cannot be precisely identified based on the current knowledge[23]. Steady-state PL spectra are presented in Figure 8. The broad emission band centered at approximately 435nm can be attributed to electron-hole recombination. In terms of intensity, CN presents the highest emission intensity followed by the pure TiO_2 catalyst. The catalysts with the highest catalytic activity in the two series (i.e. TiCN5 and TiCN5B10 composites) show a significant decrease in the PL spectral intensity as compared with the reference catalysts. This suggests that charge recombination is suppressed in the case of the composites.

To study the photogenerated charges and investigate their impact in H_2 evolution, *in-situ* EPR spectroscopy was employed. EPR spectroscopy provides high resolution information for paramagnetic centers and their environment and has been extensively applied to study photogenerated charges on TiO_2 as trapped species[13, 24]. Figure 9 presents the EPR spectra of the pristine TiO_2, B-doped TiO_2 (TiCN0B10) and the B-doped TiO_2 coupled with CN (TiCN5B10) under irradiation. Two distinct EPR signals are detected. The low-field feature, labeled *A* in Figure 9, centered at *g* ~ 2.007 most probably originates from trapped holes (h^+) species in the anatase structure [13, 24b, 25]. The broad component of the spectrum centered at high magnetic field (labeled as *B*) expands from 3380 to 3760 G and has been previously attributed to photogenerated e^- trapped at Ti^{3+} centers. The broad character is associated with the disordered environment of such paramagnetic centers at the crystal surface [13, 26].

Double integration of spectrum *B* that corresponds to surface trapped e^- reveals a difference in the actual amount of such species in the catalysts studied. The signal intensity of spectrum *B* in the TiCN0B10 and TiCN5B10 catalysts is 1.8 and 2.4 times higher than the pure TiO_2, respectively. This can originate from the formation of more photogenerated e^- in the TiCN0B10 and TiCN5B10 catalysts. The trend observed agrees with the photocatalytic activity as presented in Figure 7. It should be noted that the intensity of such species depends greatly on the illumination conditions applied and the amount of the catalyst used. Herein, the same amount of sample was used in each case. Although no detailed quantitative analysis was performed, the observed trend in Ti^{3+} signal intensity is in line with the PL data presented in Figure 8 and photocurrent measurements performed on other studies using un-doped and B-doped TiO_2 [4, 6].

In the TiCN5B10 sample, an additional set of signals centered at approximately 3308, 3404 and 3474 Gauss are detected. This feature is not observed in either the pure TiO_2 or TiCN0B10 sample. Based on their position, these EPR signals most likely do not correspond to h^+ in the anatase structure[13, 24b, 25, 27], nitric oxide (NO) or nitrogen bulk centers ($N_b^{\bullet}$) [28]. The last two cases are also excluded based on the FTIR and microscopy analysis that provide direct evidence for the stability of CN under conditions applied in the synthesis step. A possible interpretation of these new EPR features can be a Ti^{3+} center interacting with a nitrogen nucleus with *I* = 1. A theoretical spectrum obtained via computer simulation using *g* values 1.987, 1.976 and 1.96 and hyperfine values 78, 57 and 57 Gauss is given in Figure 9. Previous studies have also reported orthorhombic Ti^{3+} centers in the anatase structure[28a]. No other EPR species are considered in the simulated spectrum. This interaction can potentially originate from the coupling of TiO_2 with CN forming a composite. This interpretation is supported by the microscopy study and further suggests a strong coupling between TiO_2 and CN.

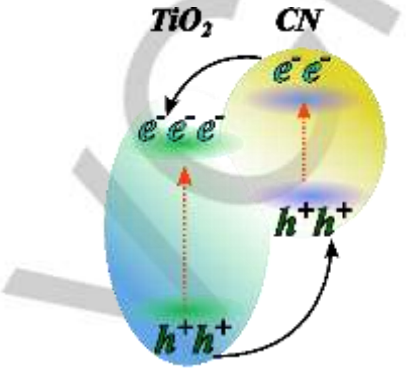

Scheme 1. Proposed charge separation mechanism in the TiO_2/CN heterojunction

Based on the above, it may be concluded that the presence of boron and CN improves the light absorption properties, improves charge recombination phenomena via efficient charge separation and, therefore, enhances charge formation. The coupling of TiO_2 and CN as revealed by TEM and the improved charge handling properties based on the PL data suggests the efficient formation of a heterojunction. Taken into account the band energy levels of TiO_2 and CN [1a, 12b, 29] a heterojunction of Type-II may be formed. Heterojunctions of Type-II are characterized by the coupling of semiconductors with correctly aligned band levels that allow spontaneous interfacial charge separation. The Conduction Band (CB) and Valence Band (VB) of the one semiconductor is positioned at more positive (or less negative) potentials than those of the second. This difference force e^- and h^+ to move at opposite directions improving charge separation. Under solar light irradiation, photogenerated e^-/h^+ pairs can be formed in both the CN and TiO_2 part of the composite based on their UV-Vis absorption spectrum. Based on the difference in band structure and in particular the actual energy level of the CB and VB in the two semiconductors, h^+ formed on the VB of TiO_2 are spontaneously transferred to the

VB of CN, while e^- in the CB of CN follow the opposite direction and are transferred to that of TiO_2 [3b, 12b]. A schematic illustration of the suggested mechanism for charge formation and separation is given in Scheme 1. Due to charge transfer through the interface of the junction formed, charge separation is favored enhancing the stability and availability of photoexcited e^-. This is essential in H_2 production and in the present work, is controlled by the modification of the TiO_2 phase and the formation of a heterojunction through the coupling of TiO_2 with CN.

Conclusions

The present study presents the development and characterization of boron-modified TiO_2 coupled with CN for the formation of heterojunctions and their application in H_2 photoproduction from aqueous ethanol solution. TiO_2 was synthesized *in-situ* in the presence of preformed CN. Modification of TiO_2 resulted in improved photoactivity. Both boron and CN content were optimized in the final composite against H_2 evolution. Materials bearing 5 wt.% CN and 10% boron presented the highest activity. The study demonstrated that the enhanced H_2 evolution originates from the improved charge handling properties as revealed by PL.

Experimental Section

Materials synthesis

Carbon nitride (CN) was synthesized via thermal polycondensation of urea (Sigma-Aldrich). 10 g of urea were dehydrated in an alumina crucible for 2 h at 150 ^oC in a muffle furnace. The alumina crucible was covered and the sample was further heated in air at 550 ^oC for 4h with a heating rate of 5 $^oC\ min^{-1}$. The obtained powder was dispersed in 0.1M HNO_3 (Sigma-Aldrich), collected via centrifugation and washed with water and ethanol three times. Finally, the light-yellow material was dried in vacuum over night at 90 ^oC.

For the synthesis of the TiO_2/CN composites a given amount of CN (0, 4, 10, 14 or 20 mg) was dispersed in ethanol and sonicated for 2 h at room temperature. To the above solution, $Ti(n\text{-}OBu)_4$ (Sigma-Aldrich) in 3.5 ml THF was added and further sonicated for 30 min at room temperature. The volume of $Ti(n\text{-}OBu)_4$ was chosen so that the theoretical final amount of CN to be 0, 2, 5, 7 and 10 wt.%. For example, 835 µl of $Ti(n\text{-}OBu)_4$ was the volume added to obtain the composite with 5 wt.% of CN. A 10% v/v% solution of H_2O in THF (final $Ti(n\text{-}OBu)_4/H_2O$ molar ratio equal to 1/100) was added dropwise followed by stirring at room temperature for 24 h. For example, 5.36 ml of H_2O were used in the synthesis of the composite containing 5 wt.% of CN. The final THF/EtOH volume ratio in all samples was kept constant and equal to 1.4. The material was collected via filtration using a 0.45 µm PTFE filter, washed with ethanol three times and dried in vacuum at 90 ^oC overnight. Finally, the material was calcined at 350 ^oC for 5 h with a heating rate of 1 $^oC\ min^{-1}$. The samples prepared were labelled as TiCN*x* were *x* denotes the nominal wt.% of CN.

For the B-doped TiO_2 / CN composite materials a similar process was adopted. The CN amount was kept constant at 5 wt.% (based on the optimized catalytic activity) and boric acid from an aqueous stock solution of 0.2 mol/L was added in the aqueous phase. The amount of boron was calculated on the basis of the molar ratio to Ti. Materials with three different nominal B/Ti molar percentages were synthesized, 5, 10 and 20%. The catalysts in this series are labelled TiCN5B*y* where *y* corresponds to the B/Ti molar percent.

Materials characterization

The amount of B present in the samples was determined by means of Inductively Coupled Plasma-Atomic Emission Spectrometry (ICP-AES). The samples were prepared by acid dissolution following the procedure reported by Wang et al.[30]. 100 mg of the sample were dissolved in a quartz crucible using 1g $(NH_4)_2SO_4$ and 2 mL of H_2SO_4 and heated until a clear solution is formed. After cooling, few drops of H_2O_2 30% and 10 mL of doubly distilled water were added. The pale turbidity observed was due to undissolved CN, which was removed by filtration on a Millipore PDVF 0.45 µm filter. The obtained solution was diluted to 100 mL with doubly distilled water for the analysis with an Optima 8000 instrument (Perkin Elmer; Waltham, MA, USA) equipped with an integrated autosampler (S10, Perkin Elmer; Waltham, MA, USA). The amounts of Ti and B were determined at the operative wavelengths (Ti 339.90 nm; B 249.677 nm) using 5-points calibration curves. The precision of the measurements as repeatability (as RSD%) for the analysis was always less than 5%.

A TGA Q500 instrument was used for the thermogravimetric analysis. Samples were heated from 100 to 800 ^oC with a heating rate of 10 $^oC\ min^{-1}$ under air flow. The weight difference between 450 and 600 ^oC was taken to calculate the composition of the nanocomposites. A Micrometrics ASAP 2020 system was used for the N_2 adsorption–desorption isotherms and analysis was performed at liquid nitrogen temperature. Samples were initially degassed at 170 ^oC overnight and specific surface area was determined using the Brunauer–Emmett–Teller (BET) model. A Perkin Elmer 2000 instrument was used to acquire the Fourier transform infrared (FT-IR) spectra using KBr pellets. A Philips X'Pert diffractometer with a Cu Ka X-ray source was used to collect the X-ray diffraction patterns. Diffuse reflectance UV-visible spectra were obtained with a PerkinElmer (Lamda 35) spectrophotometer. $BaSO_4$ was used as reference. The Kubelka-Munk function was used to estimate the band gap energies from the samples' optical absorption edges using:

$$F(R)=\frac{(1-R)^2}{2R}$$

where R is the reflectance. The E_g values were estimated by extrapolating the linear part of the plot $F(R)h\nu^{1/2}$ versus energy. TiO_2 was treated as indirect while CN as direct semiconductor.

Raman spectra were acquired after excitation with a 532 nm laser using a Renishaw instrument. Photoluminescence (PL) spectra were recorded with a Fluorolog FM-32 spectrofluorometer (Horiba Jobin Yvon) after excitation at 360 nm. The X-ray photoelectron spectroscopy (XPS) measurements were carried out in an ultrahigh vacuum (UHV) spectrometer. The Al Kα line (1486.6 eV) of a dual anode X-ray source was used as incident radiation. All spectra were recorded in constant pass energy mode (44 and 22 eV for survey and high resolution spectra, respectively). A Bruker Elexys E500 spectrometer was used to acquire spectra at X-band frequencies. EPR measurements were contacted at 5 K using a continuous flow ^4He cryostat (ESR 900, Oxford Instruments). microwave power of 0.264 mW and field modulation of 100 kHz and 5 G. The catalysts (20mg) were irradiated at 405nm directly in the cavity with 2 mW power using a diode laser (Thorlabs code DL5146-251) connected to an optical fiber with one end inserted in the EPR sample tube. Theoretical EPR spectra were obtained using the EasySpin software package[31]. Catalysts were also analyzed by Transmission Electron

Microscopy (TEM) using a Field Emission Gun JEOL2010 instrument equipped operated at 200kV. This instrument has a spatial resolution at Scherzer defocus conditions of 0.19 nm. Scanning Electron Microscopy (SEM) images were recorded on a Field Emission Gun FEI Nova 450 electron microscope with an accelerating voltage of 5 kV. Energy dispersive X-ray spectra (EDS) were obtained in the same microscope using 20 kV.

Photocatalytic activity evaluation

The photocatalytic activity in H_2 production of all catalysts was evaluated using a solar simulator (LOT-Oriel) equipped with a 150 W Xe lamp and an Atmospheric Edge Filter. A power density of approximately 25 and 180 mW cm^{-2} is achieved in the UV (300-400 nm) and in the visible region (400-1000 nm), respectively. All reactions were contacted at flow conditions (15 ml min^{-1} argon flow) over a period of 24 h[32]. The catalyst (60 mg) was suspended into 80 ml of an aqueous ethanol solution (50 v.%) and Pt (0.1 wt.%) was photodeposited as co-catalyst by adding $Pt(NO_3)_2$. Temperature was maintained at 25 °C by means of a cryostat during the reaction. The reaction mixture was purged with argon (15 ml min^{-1}) for 40 min under steering to remove air prior to irradiation. An Agilent 7890 gas chromatographer equipped with a Carboxen 1010 PLOT (Supelco, 30 m × 0.53 mm ID, 30 µm film) column using Ar as carrier followed by a Thermal Conductivity Detector (TCD) and DB-225ms column (J&W, 60 m × 0.32 mm ID, 20 µm film) using He as carrier followed by a mass spectrometer (MS) HP 5975C was used to detect the evolved gaseous products on-line.

Acknowledgements

Financial support from the French National Research Agency (ANR) under the Program “Make Our Planet Great Again” (ANR-18-MOPGA-0014) is fully acknowledged. T.M. acknowledges financial support from MIUR PRIN2017 project 2017PBXPN4.

Keywords: boron, carbon nitride, hydrogen, photocatalysis, photoreforming, TiO_2.

[1] a) K. C. Christoforidis, P. Fornasiero, *ChemCatChem* **2017**, *9*, 1523-1544; b) M. G. Walter, E. L. Warren, J. R. McKone, S. W. Boettcher, Q. Mi, E. A. Santori, N. S. Lewis, *Chem. Rev.* **2010**, *110*, 6446-6473; c) K. C. Christoforidis, P. Fornasiero, *ChemCatChem* **2019**, *11*, 368-382; d) X. Chen, S. Shen, L. Guo, S. S. Mao, *Chem. Rev.* **2010**, *110*, 6503-6570.

[2] Y. Ma, X. Wang, Y. Jia, X. Chen, H. Han, C. Li, *Chem. Rev.* **2014**, *114*, 9987-10043.

[3] a) K. C. Christoforidis, A. Iglesias-Juez, S. J. A. Figuero, M. D. Michiel, M. A. Newton, M. Fernandez-Garcia, *Catal. Sci. Technol.* **2013**, *3*, 626-634; b) L. Chen, X. Zhou, B. Jin, J. Luo, X. Xu, L.Zhang, Y. Hong, *Int. J. Hydrogen Energy* **2016**, *41*, 7292-7300.

[4] P. Carmichael, D. Hazafy, D. S. Bhachu, A. Mills, J. A. Darr, I. P. Parkin, *Phys. Chem. Chem. Phys.* **2013**, *15*, 16788-16794.

[5] a) V. Gombac, L. D. Rogatis, A. Gasparotto, G. Vicario, T. Montini, D. Barreca, G. Balducci, P. Fornasiero, E. Tondello, M. Graziania, *Chem. Phys.* **2007**, *339*, 111-123; b) S. In, A. Orlov, R. Berg, F. García, S. Pedrosa-Jimenez, M. S. Tikhov, D. S. Wright, R. M. Lambert, *J. Am. Chem. Soc.* **2007**, *129*, 13790-13791; c) M. Fittipaldi, V. Gombac, T. Montini, P. Fornasiero, M. Graziani, *Inorg. Chim. Acta* **2008**, *361*, 3980-3987.

[6] N. Lu, X. Quan, J. Li, S. Chen, H. Yu, G. Chen, *J. Phys. Chem. C* **2011**, *111*, 11836-11842.

[7] a) J. Zhang, Y. Chen, X. Wang, *Energy Environ. Sci.* **2015**, *8*, 3092-3108; b) K. C. Christoforidis, Z. Syrgiannis, V. L. Parola, T. Montini, C. Petit, E. Stathatose, R. Godin, J. R. Durrant, M. Prato, P. Fornasiero, *Nano Energy* **2018**, *50*, 468-478; c) E. M. Dias, K. C. Christoforidis, L. Francas, C. Petit, *ACS Appl. Energy Mater.* **2018**, *1*, 6524-6534; d) X. Wang, K. Maeda, A. Thomas, K. Takanabe, G. Xin, J. M. Carlsson, K. Domen, M. Antonietti, *Nat. Mater.* **2009**, *8*, 76-80; e) W. J. Ong, L. L. Tan, Y. H. Ng, S. T. Yong, S. P. Chai, *Chem. Rev.* **2016**, *116*, 7159-7329.

[8] a) J. Zhang, J. Sun, K. Maeda, K. Domen, P. Liu, M. Antonietti, X. Fu, X. Wang, *Energy Environ. Sci.* **2011**, *4*, 675-678; b) Y. Zheng, L. Lin, B. Wang, X. Wang, *Angew. Chem., Int. Ed. Engl.* **2015**, *54*, 12868-12884; c) S. Yang, Y. Gong, J. Zhang, L. Zhan, L. Ma, Z. Fang, R. Vajtai, X. Wang, P. M. Ajayan, *Adv. Mater.* **2013**, *25*, 2452-2456.

[9] a) Z. Zhao, Y. Sun, F. Dong, *Nanoscale* **2015**, *7*, 15-37; b) P. Niu, L. Zhang, G. Liu, H.-M. Cheng, *Adv. Funct. Mater.* **2012**, *22*, 4763-4770; c) X. Zhang, X. Xie, H. Wang, J. Zhang, B. Pan, Y. Xie, *J. Am. Chem. Soc.* **2013**, *135*, 18-21; d) K. C. Christoforidis, T. Montini, E. Bontempi, S. Zafeiratos, J. J. D. Jaén, P. Fornasiero, *Appl. Catal., B* **2016**, *187*, 171-180.

[10] a) X.-H. Li, M. Antonietti, *Chemical Society Reviews* **2013**, *42*, 6593-6604; b) Y.-Y. Cai, X.-H. Li, Y.-N. Zhang, X. Wei, K.-X. Wang, J.-S. Chen, *Angew. Chem., Int. Ed.* **2013**, *52*, 11822-11825; c) S. A. Ansari, M. H. Cho, *Sustainable Energy Fuels* **2017**, *1*, 510-519; d) L. Wu, Q. Li, C. Yang, X. Ma, Z. Zhang, X. Cui, *J. Mater. Chem. A* **2018**, *6*, 20947-20955 ; e) Z. Xu, C. Zhuang, Z. Zou, J. Wang, X. Xu, T. Peng, *Nano Res.* **2017**, *10*, 2193-2209.

[11] S. J. A. Moniz, S. A. Shevlin, D. J. Martin, Z.-X. Guo, J. Tang, *Energy Environ. Sci.* **2015**, *8*, 731-759.

[12] a) Z. Tong, D. Yang, T. Xiao, Y. Tian, Z. Jiang, *Chemical Engineering Journal* **2015**, *260*, 117-125; b) A. Crake, K. C. Christoforidis, R. Godin, B. Moss, A. Kafizas, S. Zafeiratos, J. R.Durrant, C. Petit, *Appl. Catal., B* **2019**, *242*, 369-378; c) B. Chai, T. Peng, J. Mao, K. Li, L. Zan, *Phys. Chem. Chem. Phys.* **2012**, *14*, 16745-16752; d) X. Fan, T. Wang, B. Gao, H. Gong, H. Xue, H. Guo, L. Song, W. Xia, X. Huang, J. He, *Langmuir* **2016**, *32*, 13322-13332.

[13] K. C. Christoforidis, M. Fernandez-Garcia, *Catal. Sci. Technol.* **2016**, *6*, 1094-1105.

[14] X. Lan, L. Wang, B. Zhang, B. Tian, J. Zhang, *Catal. Today* **2014**, *224*, 163-170.

[15] M. Fittipaldi, V. Gombac, A. Gasparotto, C. Deiana, G. Adami, D. Barreca, T. Montini, G. Martra, D. Gatteschi, P. Fornasiero, *ChemPhysChem* **2011**, *12*, 2221-2224.

[16] M. Szkoda, K. Siuzdak, A. Lisowska-Oleksiak, J. Karczewski, J. Ryl, *Electrochem. Comm.* **2015**, *60*, 212-215.

[17] K. C. Christoforidis, M. Melchionna, T. Montini, D. Papoulis, E. Stathatos, S. Zafeiratos, E. Kordouli, P. Fornasiero, *RSC Adv.* **2016**, *6*, 86617-86626.

[18] A. Crake, K. C. Christoforidis, R. Godin, B. Moss, A. Kafizas, S. Zafeiratos, J. R. Durrant, C. Petit, *Appl. Catal., B* **2019**, *242*, 369-378.

[19] M. Quesada-González, N. D. Boscher, C. J. Carmalt, I. P. Parkin, *ACS Appl. Mater. Interfaces* **2016**, *8*, 25024-25029.

[20] M. Bettinelli, V. Dallacasa, D. Falcomer, P. Fornasiero, V. Gombac, T. Montini, L. Romano, A. Speghini, *J. Hazard. Mater.* **2007**, *146*, 529-534.

[21] a) X. Zhou, B. Jin, L. Li, F. Peng, H. Wang, H. Yu, Y. Fang, *J. Mater. Chem.* **2012**, *22*, 17900-17905; b) X. Zhou, F. Peng, H. Wang, H. Yu, Y. Fang, *Chem. Commun.* **2011**, *47*, 10323-10325.

[22] M. L. Guo, X. D. Zhang, C. T. Liang, *Physica B* **2011**, *406*, 3354-3358.

[23] L. Mascaretti, V. Russo, G. Zoppellaro, A. Lucotti, C. S. Casari, S. Kment, A. Naldoni, A. L. Bassi, *J. Phys. Chem. C* **2019**, *123*, 11292-11303.

[24] a) T. Berger, M. Sterrer, O. Diwald, E. Knozinger, *ChemPhysChem* **2005**, *6*, 2104-2112; b) T. Berger, M. Sterrer, O. Diwald, E. Knozinger, D. Panayotov, T. L. Thompson, J. J. T. Yates, *J. Phys. Chem. B* **2005**, *109*, 6061-6068; c) T. Berger, M. Sterrer, S. Stankic, J. Bernardi, O. Diwald, E. Knözinger, *Mat. Sci. Eng. C Mater* **2005**, *25*, 664-668; d) M. Fittipaldi, D. Gatteschi, P. Fornasiero, *Catal. Today* **2013**, *206*, 2-11.

[25] R. Scotti, I. R. Bellobono, C. Canevali, C. Cannas, M. Catti, M. D'Arienzo, A. Musinu, S. Polizzi, M. Sommariva, A. Testino, F. Morazzoni, *Chem. Mater.* **2008**, *20*, 4051-4061.

[26] J. Biedrzycki, S. Livraghi, E. Giamello, S. Agnoli, G. Granozzi, *J. Phys. Chem. C* **2014**, *118*, 8462.

[27] a) C. P. Kumar, N. O. Gopal, T. C. Wang, M.-S. Wong, S. C. Ke, *J. Phys. Chem. B* **2006**, *110*, 5223-5229; b) S. O. Baumann, M. J. Elser, M. Auer, J. Bernardi, N. Husing, O. Diwald, *Langmuir* **2011**, *27*, 1946-1953; c) M. D'Arienzo, J. Carbajo, A. Bahamonde, M. Crippa, S. Polizzi, R. Scotti, L. Wahba, F. Morazzoni, *J. Am. Chem. Soc.* **2011**, *133*, 17652-17661; d) H.-H. Lo, N. O. Gopal, S.-C. Sheu, S.-C. Ke, *J. Phys. Chem. C* **2014**, *118*, 2877-2884.

[28] a) A. E. Giannakas, E. Seristatidou, Y. Deligiannakis, I. Konstantinou, *Appl. Catal., B* **2013**, *132-133*, 460-468; b) S. Livraghi, A. Votta, M. C. Paganini, E. Giamello, *Chem. Commun.* **2005**, 498-500; c) D. Dvoranová, M. Mazúr, I. Papailias, T. Giannakopoulou, C. Trapalis, V. Brezová, *Catalysts* **2018**, *8*, 47.

[29] a) D. O. Scanlon, C. W. Dunnill, J. Buckeridge, S. A. Shevlin, A. J. Logsdail, S. M. Woodley, C. R. A. Catlow, M. J. Powell, R. G. Palgrave, I. P. Parkin, G. W. Watson, T. W. Keal, P. Sherwood, A. Walsh, A. A. Sokol, *Nat. Mater* **2013**, *12*, 798-801; b) H.-Z. Wu, L.-M. Liu, S.-J. Zhao, *Phys. Chem. Chem. Phys.* **2014**, *16*, 3299-3304; cY. Yang, Z. Zeng, G. Zeng, D. Huang, R. Xiao, C. Zhang, C. Zhou, W. Xiong, W. Wang, M. Cheng, W. Xue, H. Guo, X. Tang, D. He, *Appl. Catal., B* **2019**, *258*, 117956.

[30] Z. Wang, Z. Ni, D. Qiu, T. Chen, G. Tao, P. Yang, *J. Anal. At. Spectrom.* **2004**, *19*, 273-276.

[31] S. Stoll, A. Schweiger, *J. Magn. Reson.* **2006**, *178*, 42-55.

[32] G. Carraro, C. Maccato, A. Gasparotto, T. Montini, S. Turner, O. I. Lebedev, V. Gombac, G. Adami, G. V. Tendeloo, D. Barreca, P. Fornasiero, *Adv. Funct. Mater.* **2014**, *24*, 372-378.

10.1002/cctc.201901703

WILEY-VCH

FULL PAPER

Photocatalytic hydrogen production is significantly improved via doping TiO_2 with boron and coupling with carbon nitride. A strong interaction between TiO_2 and carbon nitride is formed resulting to the successful formation of a heterojunction. Both doping and the formation of a heterojunction improve the electronic properties of the catalysts. The enhanced photoactivity is ascribed to the improved abundance of photogenerated electron.

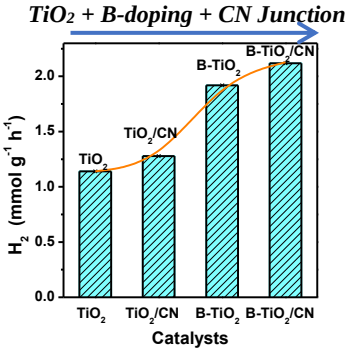

Konstantinos C. Christoforidis, Tiziano Montini, Maria Fittipaldi, Juan Josè Delgado Jaén and Paolo Fornasiero**

Page No. – Page No.

Title